Journal of CO2 Utilization 67 (2023) 102317

Contents lists available at ScienceDirect

Journal of CO2 Utilization

journal homepage: www.elsevier.com/locate/jcou

# Development of stable $La_{0.9}Ce_{0.1}NiO_3$ perovskite catalyst for enhanced photothermochemical dry reforming of methane

Zichen Du [a], Cullen Petru [a], Xiaokun Yang [b], Fan Chen [c], Siyuan Fang [d], Fuping Pan [a], Yang Gang [a], Hong-Cai Zhou [c], Yun Hang Hu [d], Ying Li [a,*]

[a] J. Mike Walker '66 Department of Mechanical Engineering, Texas A&M University, College Station, TX 77843, United States
[b] Chemistry Division, Los Alamos National Laboratory, Los Alamos, NM 87545, United States
[c] Department of Chemistry, Texas A&M University, College Station, TX 77843, United States
[d] Department of Materials Science and Engineering, Michigan Technological University, Houghton, MI 49931, United States

ARTICLE INFO

*Keywords:*
Solar-driven catalysis
Dry reforming
Perovskite
Ni-based catalyst
Ce substitution

ABSTRACT

Solar-driven photothermochemical dry reforming of methane (PTC-DRM) is a promising technique to produce syngas using greenhouse gases ($CO_2$ and $CH_4$). In this work, Ce-substituted $LaNiO_3$, i.e., $La_{1-x}Ce_xNiO_3$ perovskite catalysts were synthesized for PTC-DRM reaction under concentrated sunlight. At 700 °C under 30 suns light irradiation, the CO and $H_2$ production rates were at 616 and 620 mmol $g^{-1}$ $h^{-1}$, respectively, over the $La_{0.9}Ce_{0.1}NiO_3$ catalyst, notably higher than those obtained in dark at the same reaction temperature and higher than those over $LaNiO_3$ under the same light irradiation condition. The $CO_2$ and $CH_4$ conversion by the $La_{0.9}Ce_{0.1}NiO_3$ catalyst are among the top-performing catalysts reported in the literature. The Ce substitution of La at a small fraction ($x = 0.1$) was found to benefit Ni active sites distribution and retention of the perovskite structure, which led to mitigation of both Ni sintering and carbon formation, thus promoting light absorption and PTC-DRM activities. A higher fraction of Ce substitution ($x \geq 0.5$), however, did not show any beneficial effects. By conducting in situ DRIFTS at PTC-DRM reaction conditions and control experiment using 495 nm long-pass filter, light irradiation was found to induce photocatalytic activities on $La_{0.9}Ce_{0.1}NiO_3$ and enhance $CO_2$ adsorption and formation of active lanthanum oxycarbonates intermediates ($La_2O_2CO_3$), possibly due to the generation of oxygen vacancies and electron-hole pairs. This work reports a new catalyst design and mechanistic studies for PTC-DRM reaction, and the findings are of importance for the application low-carbon fuel generation from sunlight.

## 1. Introduction

The extensive utilization of fossil fuels for daily life and industrial applications has led to significant emissions of greenhouse gases (GHGs) including carbon dioxide ($CO_2$) and methane ($CH_4$) [1]. $CO_2$ or dry reforming of methane (DRM), which converts both GHGs into syngas ($H_2$ and CO), is an attractive process to produce sustainable fuels with low carbon emissions [2]. However, the activation and dissociation of the C═O bond in $CO_2$ and the C-H bond in $CH_4$ both require high energy input (750 kJ $mol^{-1}$ and 439.5 kJ $mol^{-1}$, respectively) [3,4]. DRM can be driven by sustainable solar energy, and efforts have been spent on researching on solar-driven thermochemical process in which solar energy is used to reach the required high temperatures [5]. On the other hand, solar-driven photothermochemical DRM (PTC-DRM) is an emerging approach that can incorporate photocatalysis into thermochemical DRM [6–9]. Compared to conventional solar thermochemical DRM process, the PTC-DRM process has a couple of additional unique aspects in utilizing light irradiation when a specially designed catalyst is applied: (1) light-driven thermocatalysis due to surface plasmon resonance effect when a plasmonic metal catalyst such as nickel is used, and (2) photo-excited electron-hole pairs from a semiconductor support that actively participate in the redox reaction [1,6,10]. Thus, by combining both thermocatalysis and photocatalysis in one reaction system, PTC-DRM activities are largely enhanced compared with traditional thermochemical DRM [1,7,9,11–13].

Metal supported on metal oxides has been one of the most widely researched catalyst structures for PTC-DRM process [14–29]. Ni is an attractive metal candidate in terms of low cost, abundance, and high

* Corresponding author.
*E-mail address:* yingli@tamu.edu (Y. Li).

https://doi.org/10.1016/j.jcou.2022.102317
Received 12 September 2022; Received in revised form 1 November 2022; Accepted 3 November 2022
Available online 10 November 2022

PTC-DRM activities [21–29]. However, high-temperature DRM environment is prone to cause Ni sintering and carbon formation, leading to deactivation of Ni-based catalysts [30]. As regard to photocatalytic DRM, which was conducted under ultraviolent or visible light irradiation at low temperatures. For example, with ultraviolet light irradiation of 150 mW/cm$^2$ at 100 °C, production rates of CO and $H_2$ can reach 750 μmol g$^{-1}$ h$^{-1}$ and 1126 μmol g$^{-1}$ h$^{-1}$, respectively on Ni-montmorillonite/$TiO_2$ [31]. With visible light irradiation of 790 mW/cm$^2$ at 400 °C, 2Ni/$CeO_{2-x}$ yielded $CH_4$ and $CO_2$ rates of 0.21 and 0.75 mmol ($g_{cat}$ • min)$^{-1}$, respectively [32]. However, these works achieved low reaction rates, far from industrial application requirements, thus exploring photocatalysts for more efficient photothermal reaction under high temperature and full-spectrum solar irradiation is very necessary.

On the other hand, adjustable bulk and surface components of metal oxides, such as perovskite oxides of general formula $ABO_3$, is a promising catalyst candidate [33]. In the perovskite oxide framework, the A-site is generally a rare earth or alkaline earth metal, such as La [34–37] and Sr [38], while transient metal, such as Ni [34,35,37] and Co [39] can occupy B-site. Compared to a metal oxide-supported metal catalyst system, perovskite oxides have the advantages of uniform dispersion of active metal sites and highly tunable oxygen vacancies concentration, thus can counter deactivation [34,35]. Another beneficial advantage of the perovskite oxide catalyst is its considerable photocatalytic activity due to a desirable narrow band gap (e.g., $LaNiO_3$: ~2.2 eV) [40,41]. This makes perovskite oxides also attractive in the field of photocatalytic organic compounds degradation, water splitting and $N_2$ fixation [42–44]. From existing research, the base perovskite structure, $LaNiO_3$, was reported to decompose completely during the DRM reaction, and Ni-$La_2O_3$ alone was unable to resist Ni sintering and carbon deposition, thus resulting in inefficient DRM reaction [36,45]. Partial substitution at the A-site of perovskite presents an effective approach, as this modification may remarkably enhance the catalytic activities by altering the electronic state of B-site cations and/or introducing oxygen vacancies [46], thus both average Ni oxidation states and Ni particle size will be reduced, and carbon deposition can be suppressed. Wang et al. reported that Ce substitution at the A-site of $LaNi_{0.5}Fe_{0.5}O_3$ perovskite introduced more oxygen vacancies and activated B-site cations, thus the DRM activity was enhanced [36]. Valderrama et al. also reported that partial substitution of La by Sr at A-site in $LaCoO_3$ structure improved Co metallic phase dispersion, leading to high DRM activities and coke resistance [47]. Therefore, $LaNiO_3$ perovskite catalyst with partial substitution at A-site can be a promising candidate for enhanced PTC-DRM performance due to its photoactivity and enhanced properties to resist metal sintering and coke deposition.

This work aims to conduct a systematic exploration of efficient PTC-DRM activities and mechanism studies over efficient $La_{1-x}Ce_xNiO_3$ catalysts (x = 0.0 – 1.0). The catalyst morphology, surface chemical states of catalysts before and after PTC-DRM reaction, and optical properties of fresh catalysts were characterized to understand the promoting effects. Then, the in situ diffuse reflectance infrared Fourier transform spectroscopy (in situ DRIFTS) was performed on the catalysts within the temperature range of 25–600 °C under light and dark conditions to understand the intermediate change relation with the catalyst activities. Finally, the roles of each component of PTC-DRM were discussed to understand the PTC-DRM mechanism.

## 2. Experimental

### 2.1. Catalyst synthesis

$La_{1-x}Ce_xNiO_3$ catalysts were synthesized by the Pechini method [48], and the corresponding metal nitrates were utilized with appropriate stoichiometry. Specifically, to synthesize $La_{0.9}Ce_{0.1}NiO_3$, 79.9 mg $La(NO_3)_3$•6 $H_2O$, 8.9 mg $Ce(NO_3)_3$•6 $H_2O$ and 59.6 mg $Ni(NO_3)_2$•6 $H_2O$ along with 78.8 mg citric acid were dissolved in 5 ml water at a metal cations to citric acid ratio of 1:1, denoted as solution A. Another 78.8 mg citric acid was dissolved in 2 ml ethylene glycol and denoted as solution B. Solution B was added dropwise to solution A. The resulting solution was stirred for 15 min at 400 rpm and was then heated to 120 °C to form a viscous gel and finally yielded a solid precursor. This product was then transferred to an oven to be calcinated under air at 750 °C for 5 h to produce the corresponding catalyst samples.

### 2.2. Catalyst characterization

Morphology, structure, and composition of the catalysts were characterized by transmission electron microscopy (TEM, FEI Tecnai G2 F20ST), high-angle angular dark-field scanning transmission electron microscopy (Hitachi 2700 C), X-ray diffraction (XRD, BRIKER D8), and X-ray photoelectron spectroscopy (XPS, Omicron), Raman spectroscopy (Horiba Jobin-Yvon LabRam HR, 633 nm laser source). UV–vis diffuse reflectance spectra were collected by a Hitachi U4100 UV–vis–NIR Spectrophotometer with Praying Mantis accessory. *In situ* diffuse reflectance infrared Fourier transform spectroscopy (DRIFTS) spectra were collected on a Nicolet 6700 infrared spectrometer (Thermo Electron) equipped with a Praying Mantis DRIFTS accessory and a reaction chamber (Harrick Scientific, HVC-DRP). The maximum allowable operating temperature of the chamber is 600 °C. Because PTC-DRM activities were evaluated after reducing catalysts in $H_2$/Ar mixture at 700 °C for 2 h, TEM, XRD, XPS, UV–vis characterization was conducted on $H_2$-reduced catalysts. $H_2$ temperature-programmed reduction ($H_2$-TPR, Micromeritics, AutoChem II 2920) was performed on 0.15 g fresh catalysts under a 10% $H_2$/90% Ar gas flow of 40 standard cubic centimeters per min (sccm) with a heating rate of 10 °C/min from 200° to 700°C. The thermogravimetric analysis (METTLER TOLEDO, TGA) was performed on 20 mg spent catalysts under an air flow of 40 sccm with a heating rate of 10 °C/min from 25° to 800°C and kept at 800 °C for 3 h.

### 2.3. PTC-DRM performance measurements

A similar experimental setup applied in the PTC-DRM performance measurements was reported in our previous works [14,16,49], and the reactor configuration is shown in Fig. S1. The concentrated solar irradiation can be operated as high as 1200 W, and the corresponding light intensity was measured to be 3.6 W/cm$^2$ (Fig. S2), which resulted in 420 °C on the catalyst surface. Auxiliary heat was supplied from a tube furnace to reach higher temperatures. A thermocouple was in contact with the center of the catalyst surface and connected to the furnace to provide feedback to the heating program, thus ensuring catalyst surface temperature was the same under light and dark conditions once a designated temperature was set. For PTC-DRM experiments, 5 mg catalyst was dispersed in 5 ml deionized water and sonicated to form a uniform ink. The ink was then dropped onto a piece of Whatman™ Quartz filter paper and placed on the catalyst holder and transferred into the tube reactor. The reactor was first purged with 150 sccm Ar for 30 min to remove impurities under room temperature, followed by reducing the catalyst under a mixed flow of 23 sccm $H_2$ and 28 sccm Ar for 1 h at 700 °C. Then, the reactor was purged with 150 sccm Ar to remove the remaining $H_2$. After that, the reactant gases (10% $CO_2$/10% $CH_4$/80% Ar) were introduced into the reactor with a flow rate of 14 sccm. Only CO and $H_2$ were detected as the products by an on-line gas chromatograph (GC 2010, Shimadzu) equipped with a thermal conductivity detector (TCD) and a methanizer-assisted flame ionization detector (FID). The production rates of CO and $H_2$ ($n$, mol g$^{-1}$ h$^{-1}$) were calculated using the following formula:

$$n = \frac{P \bullet V \bullet v_i}{m \bullet R \bullet T} \bullet 3600$$

Where $P$ is the pressure (1.01 ×10$^5$ pa), $V$ is the gas volumetric flow rate (2.3 × 10$^{-7}$ m$^3$ s$^{-1}$), $v_i$ is the volume concentration of each gas, which is converted from GC measurements and calibration, $T$ is the temperature

(298.15 K), $R$ is the gas constant (8.314 J $mol^{-1}$ $K^{-1}$), and $m$ is the loaded catalyst weight ($5 \times 10^{-3}$ g).

The $CO_2$ and $CH_4$ conversion % were calculated using the following formula:

$$Conversion \quad \% = \frac{[X]_{in} - [X]_{out}}{[X]_{in}} \times 100$$

Where $[X]_{in}$ is the concentration of each original reactant gas ($CO_2$, $CH_4$), and $[X]_{out}$ is the measured concentration of each gas at the outlet.

### 2.4. In situ diffuse reflectance infrared Fourier transform spectroscopy (in situ DRIFTS) experiments

*In situ* DRIFTS spectra were recorded on a Nicolet 6700 spectrometer (Thermo Electron) equipped with a liquid nitrogen cooled HgCdTe (MCT) detector, a Praying Mantis DRIFTS accessory and a reaction chamber (Harrick Scientific, HVC-DRP) [16]. The reaction cell was equipped with a sample cup to load powder samples and a heater and temperature controller to control the reaction temperature. The maximum operation temperature of the reaction chamber is 600 °C. The dome of the DRIFTS cell has two ZnSe windows allowing IR transmission and a third (quartz) window allowing transmission of light irradiation. Light was introduced into the DRIFTS cell through an optical fiber connected to the solar simulator operated at 1200 W. The intensity of the light measured at the outlet optical fiber was close to 0.1 W/$cm^2$. After loading 10 mg of catalyst sample on the sample cup, the sample was first reduced with a gas mixture of 23 sccm $H_2$ and 28 sccm Ar for 10 min at 600 °C, and no spectra change was observed, meaning the complete reduction of the catalyst occurred. After the reduction process, the reaction chamber was cooled down to room temperature and simultaneously purged by Ar. The reaction temperature was then set to targeted temperatures (25–600 °C) with either light or dark condition, and at the same time, DRM gases were introduced. The DRIFTS data were then taken continuously until no spectra change was observed (10 min). The final DRIFTS spectra were collected and presented.

## 3. Results and discussion

### 3.1. Reducibility, crystalline structure, and morphology characterization

Reducibility of the catalyst determines the active form of the catalyst [46], thus as-prepared fully oxidized catalysts were examined by $H_2$ temperature-programmed reduction ($H_2$-TPR) analysis (Fig. 1). For $LaNiO_3$, the reduction was observed to happen in 3 steps, as the peaks appeared at 262 and 382 °C along with a broad peak ranging from 457° to 613 °C. The peaks can be associated with different intermediary species of Ni, and $La_2O_3$, as the possible reduction steps of perovskite structures are as follows [50–52]:

$$2LaNiO_3 + H_2 \rightarrow La_2Ni_2O_5 + H_2O \quad (1)$$

$$La_2Ni_2O_5 + 2\ H_2 \rightarrow La_2O_3 + 2Ni + 2\ H_2O \quad (2)$$

In general, the lowest-temperature peak is associated with reduction of $Ni^{3+}$ to $Ni^{2+}$, and the peaks at higher temperatures are due to the reduction of $Ni^{2+}$ into $Ni^{0+}$ and partial reduction of $Ce^{4+}$ or $La^{3+}$. The reduction peaks of $La_{0.9}Ce_{0.1}NiO_3$ shifted to lower temperatures, namely, 357 °C and 486 °C, corresponding very well with previous literature findings [50,53]. This result showed that the partial Ce substitution promoted the reaction between $H_2$ molecules and NiO species to occur at lower temperatures. It is likely the partial incorporation of Ce in perovskite lattice resulted in the distortion of the perovskite structure [54], thus making the reduction of perovskite easier. Additionally, the overall $H_2$ consumption was measured to increase from 2327 μmol/g on $LaNiO_3$ to 3310 μmol/g on $La_{0.9}Ce_{0.1}NiO_3$, thus indicating surface oxygen species and bulk lattice oxygen amounts being higher on

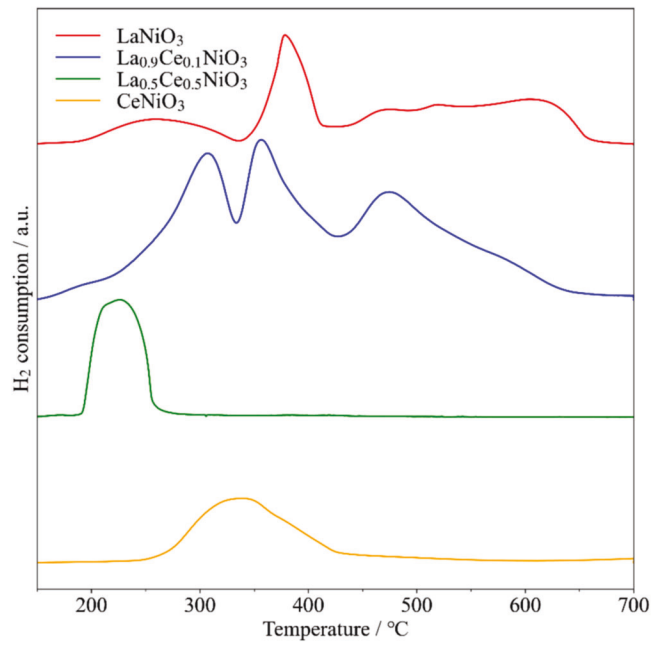


**Fig. 1.** $H_2$-TPR profiles of calcined $La_{1-x}Ce_xNiO_3$ (x = 0.0, 0.1, 0.5, 1.0).

$La_{0.9}Ce_{0.1}NiO_3$, which demonstrated an enhanced oxygen mobility upon Ce substitution [55]. On the other hand, $La_{0.5}Ce_{0.5}NiO_3$ and $CeNiO_3$ have only one reduction peak, which is likely due to the reduction of NiO and partial reduction of ceria-based oxides [56]. By calculating the total oxygen storage capacity (OSC) of each catalyst (Table S1), it was found the existence of Ce increased the total OSC on all $La_{1-x}Ce_xNiO_3$ (x = 0.1, 0.5, 1.0) catalysts compared with $LaNiO_3$. It was also observed that at 700 °C, both catalysts have been completely reduced. Therefore, 700 °C was chosen as the reduction temperature to fully reduce Ni.

X-ray diffraction (XRD) patterns of reduced catalysts were then characterized and presented in Fig. 2. For all catalysts, the absence of NiO (JCPDS 89–3080) and presence of Ni (JCPDS 04–0850) indicated

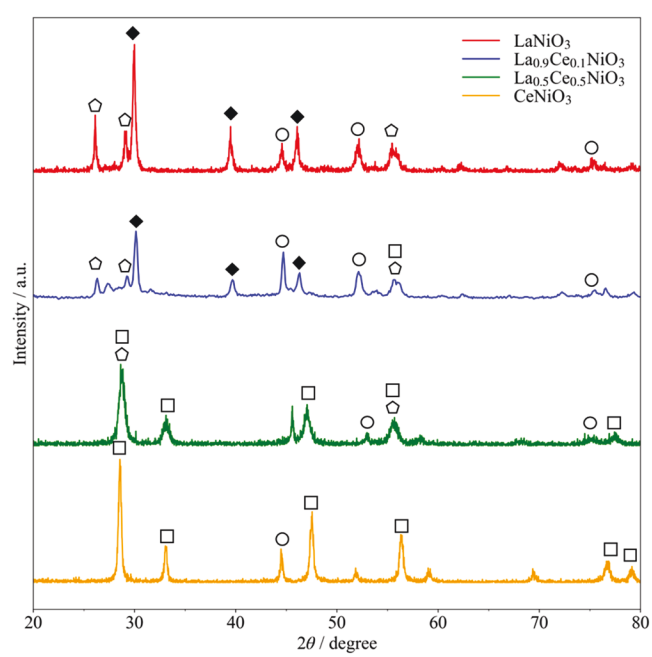


**Fig. 2.** XRD patterns of reduced $La_{1-x}Ce_xNiO_3$ (x = 0.0, 0.1, 0.5, 1.0) with the reference phase: $LaNiO_3$ (◆- JCPDS 33–0711), Ni (○- JCPDS 04–0850), $La_2O_3$ (⬠- JCPDS 71–5408), $CeO_2$ (□- JCPDS 81–9325).

that Ni element has been fully reduced, thus can act as the active metallic sites for DRM [9], which agrees with the $H_2$-TPR profiles. In addition, for $La_{1-x}Ce_xNiO_3$ with x = 0.0, 0.1, 0.5, $La_2O_3$ (JCPDS 71–5408) peaks are clearly resolved. $CeO_2$ (JCPDS 81–9325) was weakly observed on $La_{0.9}Ce_{0.1}NiO_3$, which is likely due to the relatively low concentration and uniform distribution of $CeO_2$. Peaks at 2θ of 30.2°, 39.7°, and 47.4°, characteristic of $LaNiO_3$ structure (JCPDS 33–0711) [57,58], have been only identified on x = 0.0 and 0.1 samples. Wang et al. proposed the "self-regeneration" effect that Ce cations ($Ce^{3+}/Ce^{4+}$) will reversibly shuttle between $CeO_2$ and perovskite structure depending on the local redox fluctuations [36]. The absence of perovskite structure on $La_{0.5}Ce_{0.5}NiO_3$ is likely due to its transition to $CeO_2$. For $CeNiO_3$ sample, only Ni and $CeO_2$ phases are identified. These results revealed the existence of perovskite structure only on $LaNiO_3$ and $La_{0.9}Ce_{0.1}NiO_3$.

Transmission electron microscopy (TEM) and energy dispersive X-ray spectrometry (EDS) tests were then conducted on the reduced $La_{1-x}Ce_xNiO_3$ samples to investigate the morphology and elemental compositions (Fig. 3). The EDS elemental mapping evidenced the presence of each element (actual metal atomic fraction listed in Table S2) and demonstrated the uniform distribution of La and Ce elements. It is widely accepted that small particle size highly benefits the coking resistance and light absorption properties of Ni-based catalysts for the DRM process [59]. While most of the particle sizes ranged from 5 nm to 40 nm, with higher Ce substitution, the average Ni particle size gradually increased. Specifically, the average particle sizes increased from 12.3 ± 5.7 nm on $LaNiO_3$ to 22.3 ± 8.0 nm on $CeNiO_3$. In addition, $La_{0.5}Ce_{0.5}NiO_3$ showed clearly separate and large metallic Ni particles. The appearance of the Ni particles is likely due to the weak interaction with the $La_2O_3$ and $CeO_2$ with an excess amount of Ce substitution. Moon et al. also reported on $La_{0.5}Ce_{0.5}NiO_3$, segregated phases of singular NiO, $CeO_2$, and $La_2O_3$ were observed, and poor activities of steam $CO_2$ reforming of $CH_4$ were received due to the weak metal-support interaction [50]. These results confirmed that Ni distribution is optimal on $La_{0.9}Ce_{0.1}NiO_3$ among these samples.

Perovskite structure materials are reported to desorb part of the lattice oxygen at high temperature in the reducing environment; concurrently oxygen vacancies ($V_O$) will be formed and partial valence change of the B-site ions will happen [60]. The oxygen vacancies have been generally believed to benefit DRM performance in both $CO_2$ adsorption and coke mitigation [12,61]. The dissociation of C-O of $CO_2$ can happen on the $V_O$ then produce CO and O, in which O becomes mobile and can thus participate in the removal of deposited coke by oxidizing C into CO [62]. Therefore, X-ray photoelectron spectroscopy (XPS) analyses were conducted on reduced $La_{0.9}Ce_{0.1}NiO_3$ and $LaNiO_3$ catalysts to investigate the surface elemental compositions. XPS analysis of La (830 ~ 860 eV), Ni (850 ~ 880 eV) and Ce (880 ~ 925 eV) were not discussed as the peaks of these three elements overlap, making it impractical to reach meaningful conclusions. O 1 s deconvolution was then performed in Fig. 4, and two types of oxygen species were located, lattice oxygen ($O_L$) at ~530 eV, and chemisorbed oxygen ($O_A$) related to the presence of oxygen vacancies ($V_O$) at ~532 eV [63]. The $O_A$

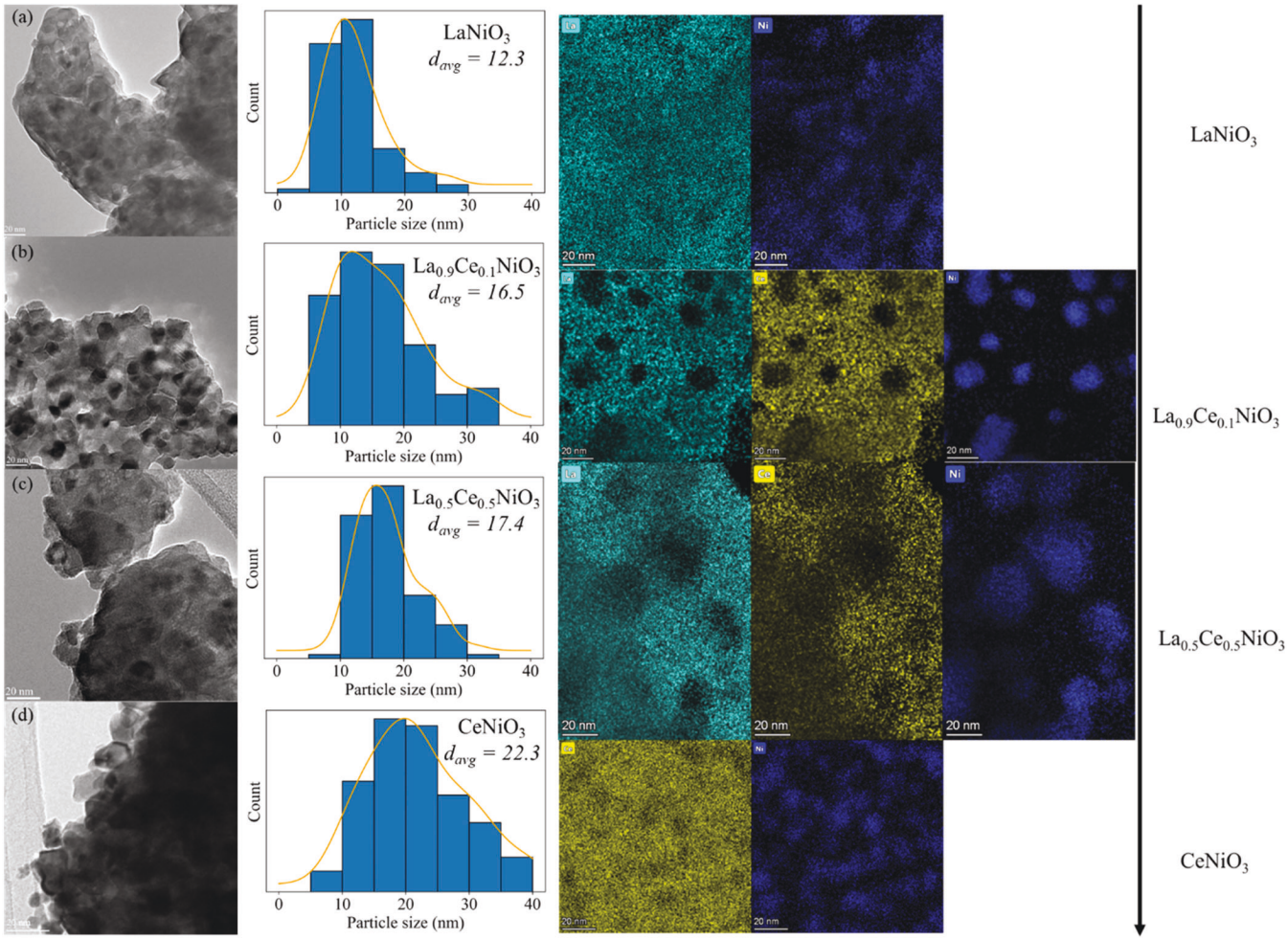


**Fig. 3.** TEM images, Ni particle size distributions, and EDS elemental mapping images of reduced $La_{1-x}Ce_xNiO_3$ samples: (a) $LaNiO_3$, (b) $La_{0.9}Ce_{0.1}NiO_3$, (c) $La_{0.5}Ce_{0.5}NiO_3$, (d) $CeNiO_3$ (The Ni particle size distributions are statistically analyzed over 100 particles for each sample).

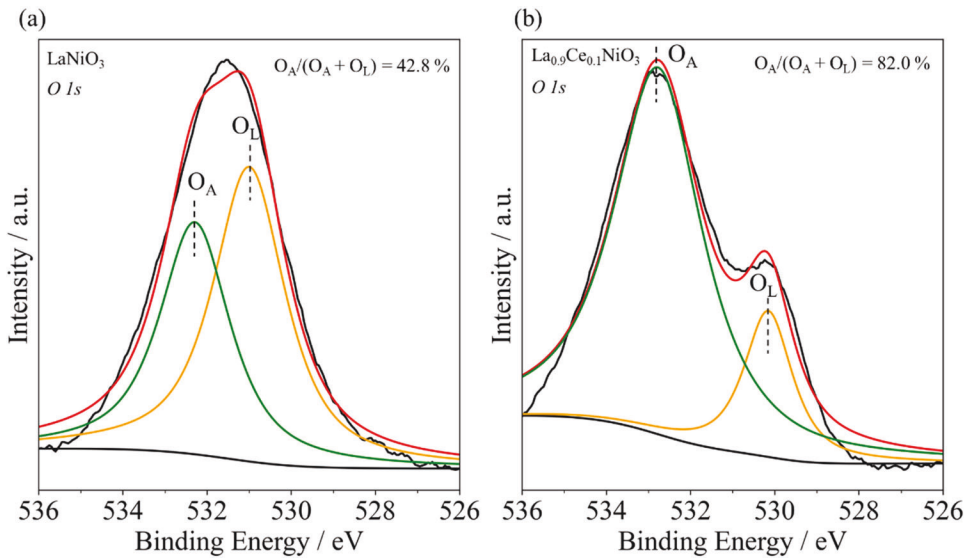


**Fig. 4.** Deconvolution of O 1 s XPS spectra of reduced (a) $LaNiO_3$ and (b) $La_{0.9}Ce_{0.1}NiO_3$ catalysts.

concentration was calculated as the peak area ratio of $O_A$, and the values on $LaNiO_3$ and $La_{0.9}Ce_{0.1}NiO_3$ were 42.8% and 82.0%, respectively. Therefore, the partial Ce substitution clearly introduces more $V_O$ on the reduced catalyst.

The optical properties were then characterized by UV–vis absorption spectra (Fig. 5). All catalysts showed strong UV light absorption abilities, and the band gaps of $LaNiO_3$, $La_{0.5}Ce_{0.5}NiO_3$, $CeNiO_3$ were calculated to be 2.19 eV, 2.94 eV, and 2.76 eV, respectively, demonstrating their semiconductor properties. However, according to the Tauc plot of $La_{0.9}Ce_{0.1}NiO_3$, it is not plausible to determine the band gap value. $LaNiO_3$ and $CeNiO_3$ showed very similar light absorption across the wavelength range from 200 to 800 nm and a characteristic adsorption peak centered at around 280 nm was identified, which is similar to reported absorption curves [64,65]. $La_{0.9}Ce_{0.1}NiO_3$ expressed strongest light absorption ability, especially across visible light wavelength range. The reason is likely due to the small and well-distributed Ni particles (indicated by TEM and EDS) since black Ni particles have a dominating light absorption ability and hinder the light transmission to other components [22].

### 3.2. Evaluation of PTC-DRM activities

The PTC-DRM activities on $La_{1-x}Ce_xNiO_3$ (with x = 0.0–1.0) were evaluated at 700 °C under illumination by a 1200 W concentrated solar simulator and were compared at the same temperature under dark conditions. The results are presented in Fig. 6 and Fig. S3. All catalysts showed DRM performance enhancement under light conditions compared with those under dark conditions, demonstrating the photo-active nature of perovskite catalysts. It was found that with a small amount of Ce substitution (0.1, 0.3), the PTC-DRM activities were largely enhanced. By comparing $LaNiO_3$ and $La_{0.9}Ce_{0.1}NiO_3$, the average CO and $H_2$ production rates increased from 363 mmol $g^{-1}$ $h^{-1}$ and 258 mmol $g^{-1}$ $h^{-1}$ to 550 and 545 mmol $g^{-1}$ $h^{-1}$ in the dark with Ce substitution, while under light illumination, the average CO and $H_2$ production rates even increased from 468 mmol $g^{-1}$ $h^{-1}$ and 395 mmol $g^{-1}$ $h^{-1}$ to 616 mmol $g^{-1}$ $h^{-1}$ and 620 mmol $g^{-1}$ $h^{-1}$.

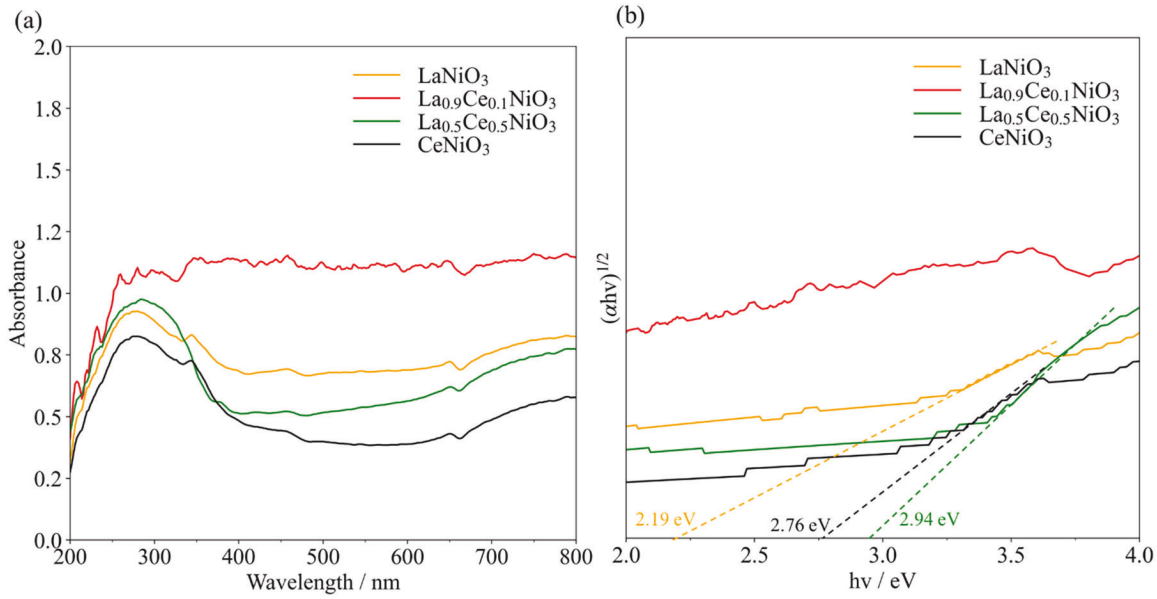


**Fig. 5.** (a) UV–vis absorption spectra and (b) band gap measurement using Tauc plot of the $La_{1-x}Ce_xNiO_3$ materials.

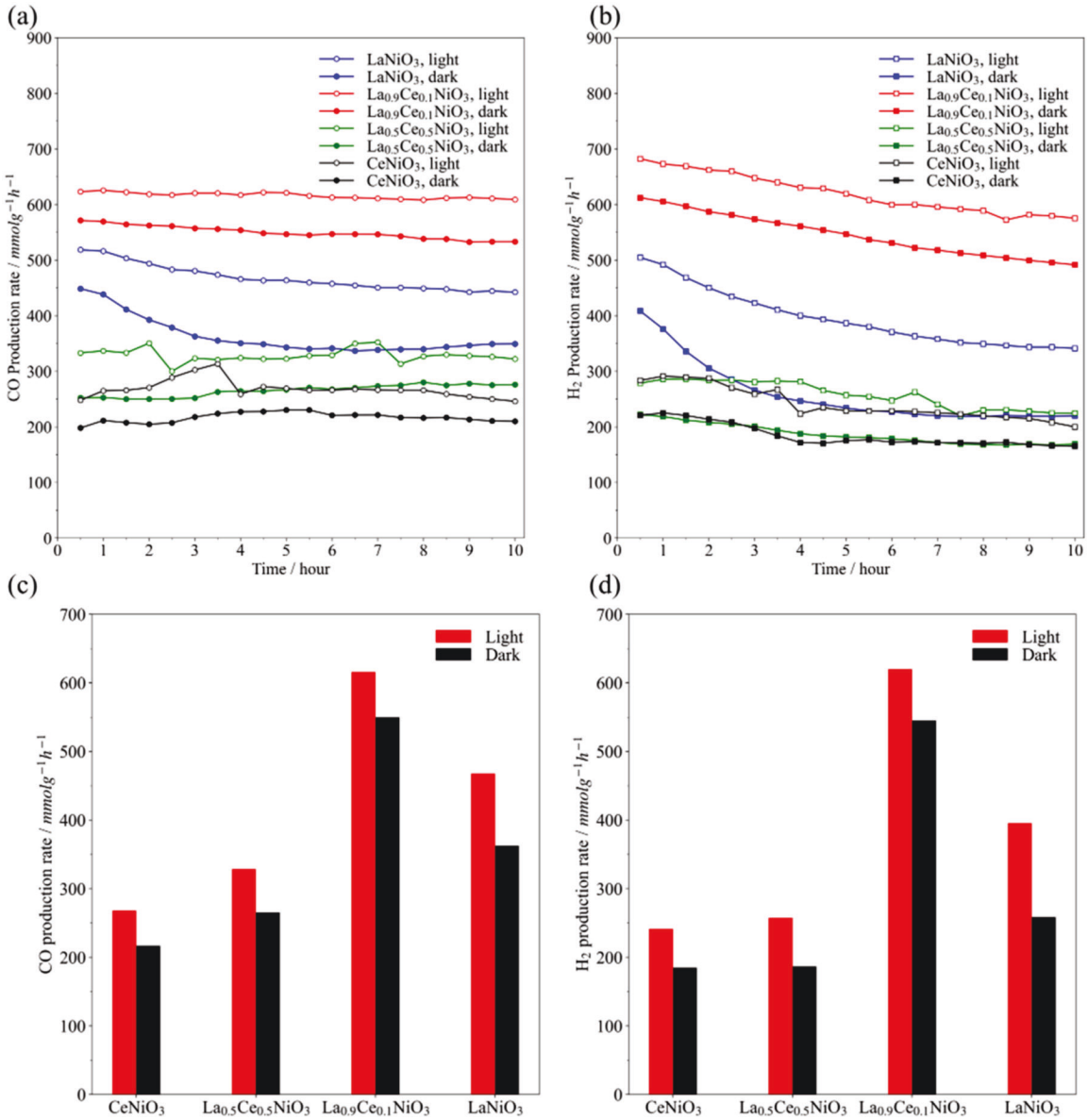


**Fig. 6.** (a and b) 10 h stability for CO and $H_2$ production rate on $La_{1-x}Ce_xNiO_3$ (with x = 0.0–1.0) at 700 °C; (c and d) average CO and $H_2$ production rates.

However, when Ce concentration is rich (x = 0.5 and x = 1.0), the performance of the catalyst did not further increase. Wang et al. [36] reported the similar catalyst performance as the function of the Ce substitution degree on $La_{1-x}Ce_xNi_{0.5}Fe_{0.5}O_3$ and suggested that Ni phase provides the primary catalytic activity, and the (LaCe)(NiFe)$O_3$ perovskite further enhances the catalytic activity, while $CeO_2$ is not responsible for the activity enhancement.

It was also observed that CO production rates are more stable than $H_2$ production rates during the reaction time. Specifically, on $La_{0.9}Ce_{0.1}NiO_3$ under light condition, the 10th-h CO production rate was only 2.23% less than initial value, while $H_2$ production rate showed a 15.7% decrease. The $CH_4$ conversion rate also decreased relatively faster than $CO_2$ (Fig. S4). These results may be attributed to the consumption of the Ni active sites for $CH_4$ conversion to produce $H_2$ and the sufficient concentration of $V_o$ active sites for $CO_2$ conversion to produce CO [12].

Ultimately, $La_{0.9}Ce_{0.1}NiO_3$ exhibited good catalytic DRM stability in both light and dark conditions. Furthermore, it was found that $La_{0.9}Ce_{0.1}NiO_3$ produced an average $H_2$/CO ratio of 1.01 under light conditions, which is optimal in achieving near-unity syngas production. Overall, these results present the promotional effects of Ce substitution and light illumination to improve both activity and stability for DRM.

In our previous studies, we have conducted PTC-DRM on both Pt-based and Ni-based catalysts [7,8,12,49]. Comparing the Pt-based and Ni-based catalysts, the required loading of Ni is generally larger than Pt to achieve optimal DRM activity. However, under photo-illumination when electron-hole pairs are generated, the too large an amount of metal may result in a stronger charge recombination, leading to a lower photocatalytic contribution [22,66,67]. We further compared this work with the state-of-the-art results in the literature, including both PTC-DRM and DRM. In literature, different light sources and formats of results were reported (e.g., $H_2$ and CO production rates, $CO_2$ and $CH_4$ consumption rates, average $CO_2$ and $CH_4$ conversion percentage, etc.), thus making it difficult to compare the performance directly. However, from Table 1, it is still clear to see the $La_{0.9}Ce_{0.1}NiO_3$ catalyst ranks among the top ones in terms of average $CO_2$ and $CH_4$ conversion percentages.

### 3.3. *In situ DRIFTS analysis*

*In situ* diffuse reflectance infrared Fourier transform spectroscopy

**Table 1**
Comparison of the conversion of $CO_2$ and $CH_4$ of $La_{0.9}Ce_{0.1}NiO_3$ catalysts with the literature data.

| Catalyst | Temp (°C) | Conversion (%) | | Reference |
|---|---|---|---|---|
| | | $CO_2$ | $CH_4$ | |
| $La_{0.9}Ce_{0.1}NiO_3$ | 700 | 70.8 | 80.0 | This work |
| Ni/mesoporous $TiO_2$ | 600 | 44.4 | 48.7 | [11] |
| $(Ni/CeO_2)@SiO_2$ | 800 | 80 | 66 | [9] |
| $Pt/TiO_2$ | 700 | 62 | N/A | [68] |
| $MgO/Pt/Zn\text{-}CeO_2$ | 600 | 52.6 | 38.8 | [12] |
| Pt/mesoporous $TiO_2$ | 500 | 0.23 | 0.22 | [69] |
| $Ni/CeO_{2-x}$ | 500 | N/A | 10 | [32] |
| Ni-Fe/MgO | 760 | 70 | 63 | [70] |
| Ni-Cu/Mg(Al)O | 600 | 60 | 47 | [71] |
| $SiO_2$ @Ni@$ZrO_2$ | 700 | 48.8 | 43.1 | [72] |
| Ni-Cu/$SiO_2$ | 800 | 84.5 | 77.5 | [73] |

(DRIFTS) analysis was conducted to investigate the intermediates' change under concentrated solar irradiation or in the dark conditions in the DRM reactant gas atmosphere at temperatures ranging from room temperature (25 °C) to maximum operating temperature (600 °C) (Fig. S5). Upon exposure to the $CO_2$ and $CH_4$, several peaks were observed. According to previous reports, the peaks centered at 3016 $cm^{-1}$, 1338 $cm^{-1}$, and 1308 $cm^{-1}$ were identified as gaseous $CH_4$ [74], and the broad peak centered at 2313 $cm^{-1}$ was identified as gaseous $CO_2$ [75]. The peak intensities of gaseous $CH_4$ and $CO_2$ were observed to decrease as temperature increased, indicating the endothermic characteristic of DRM. The adsorption bands located at 2178 $cm^{-1}$ and 2111 $cm^{-1}$ are assigned to gaseous CO [76,77], which appeared only after 400 °C in the dark, but was observed starting from 200 °C under light, indicating that light irradiation can activate the CO production at lower temperature.

To clearly observe the intermediates' change, the in situ DRIFTS spectra at the wavenumber ranging from 1200 to 2000 $cm^{-1}$ are presented in Fig. 7. It was observed that the solar irradiation led to an intensity increase in formate, m-$CO_3^{2-}$, and b-$CO_3^{2-}$ bands, which are all active intermediates in $CO_2$ reduction reactions [78,79]. The stronger peak intensities under light are likely due to the generation of $V_O$ under light that promoted $CO_2$ adsorption and formation of these peaks [8,49].

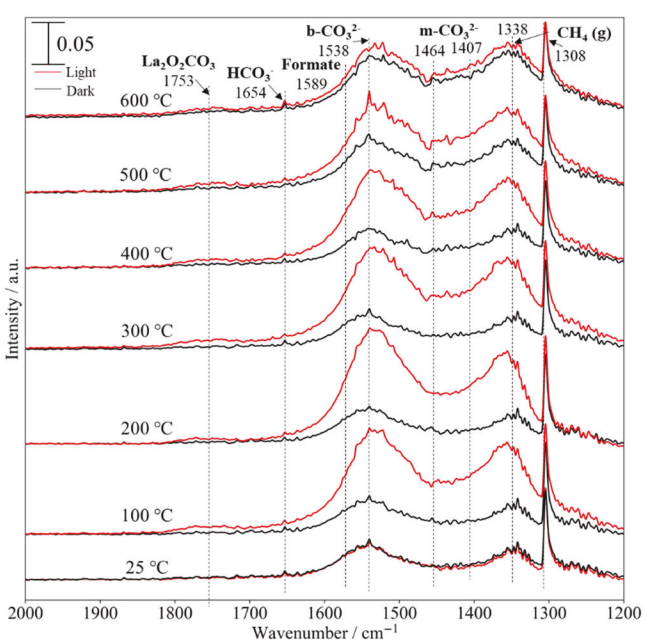


**Fig. 7.** In situ DRIFTS spectra of $La_{0.9}Ce_{0.1}NiO_3$ under DRM reaction conditions under light and in the dark conditions at temperatures ranging from 25° to 600°C.

This aligns with the promoted reaction rates in the DRM process under light irradiation.

It was also noticed that under light condition, the peak at 1753 $cm^{-1}$, which is attributed to $La_2O_2CO_3$ species [80], only appeared under light irradiation when temperature was between 100 and 600 °C. As previously reported, two parallel routes for $CO_2$ activation may be occurring on the La-based catalysts: (1) Through direct decomposition on oxygen vacancies and (2) Through the formation and decomposition of $La_2O_2CO_3$ [60,81]. Thus, $La_2O_2CO_3$ has been widely recognized to be an active intermediate formed by the reaction between $La_2O_3$ and $CO_2$, further reacting with carbonaceous intermediates on Ni at the metal-support interface to produce CO and regenerate the $La_2O_3$. The generation of $La_2O_2CO_3$ under light irradiation aligns well with the higher DRM activities. Similarly, Akula et al. also observed the formation of $La_2O_2CO_3$ on $La_2O_3/TiO_2$ during photocatalytic water splitting reaction, which can highly improve the photo-induced electro-hole pairs separation and speed up the photocatalytic methanol decomposition [82]. Gao et al. also reported the presence of $La_2O_2CO_3$ during the PTC-DRM process, which can facilitate the coke mitigation on metal surface [83].

All the carbonate peaks intensities are also weaker on $LaNiO_3$, and $La_2O_2CO_3$ was not observed on the Ce free sample (Fig. S6). This result indicated that partial Ce substitution can benefit the adsorption of $CO_2$ and formation of $La_2O_2CO_3$ upon light irradiation. It is likely that the rich $V_O$ density from the partial Ce substitution boosted the generation of intermediates.

### 3.4. Spent catalyst characterization

Characterization of spent catalysts was conducted to reveal information about catalyst stability, as both Ni sintering and coke formation are generally believed to be responsible for deterioration of DRM performance [59]. TEM measurements were first carried out on spent $LaNiO_3$ and $La_{0.9}Ce_{0.1}NiO_3$ after 10 h DRM reaction at 700 °C under the dark and light conditions (Fig. 8). By comparing these TEM images with Fig. 3, Ni sintering can be observed on the spent $LaNiO_3$ after DRM reaction at 700 °C under both dark and light conditions (large Ni particles are circled in Fig. 8), while no obvious Ni sintering was observed on the spent $La_{0.9}Ce_{0.1}NiO_3$. To quantify the extent of Ni sintering, we analyzed the Ni particle size distribution over 100 particles for each spent sample and presented in Fig. S7. Ni with much larger particle sizes were clearly observed on spent $LaNiO_3$ (average value of 32.0 ± 14.8 nm and 37.6 ± 17.1 nm for light and dark, respectively), while $La_{0.9}Ce_{0.1}NiO_3$ showed much smaller values (average value of 23.2 ± 6.3 nm and 25.0 ± 8.4 nm for light and dark, respectively), which matched the PTC-DRM performance difference presented in Fig. 6. These results suggest that the presence of Ce benefited Ni stabilization, and mitigated Ni sintering, resulting in better PTC-DRM performance on $La_{0.9}Ce_{0.1}NiO_3$. As widely reported, Ce-containing Ni-based catalysts showed strong metal support interactions that prevented Ni from sintering and deactivating [84–86]. However, no obvious differences were observed on both catalysts between light and dark conditions, meaning the Ni sintering is mainly the result of thermal stability and independent of light conditions.

Large amounts of carbon filaments (e.g., CNTs) were clearly observed on both samples under dark conditions, yet under light conditions, the coke species were mainly active carbon. We conducted further analyses of additional TEM images of spent $LaNiO_3$ and $La_{0.9}Ce_{0.1}NiO_3$ after DRM reaction at 700 °C under the dark condition (Fig. S8). It was observed that on $La_{0.9}Ce_{0.1}NiO_3$, the majority of Ni particles were still closely attached to the supports, whereas, on $LaNiO_3$, many Ni particles were detached from the support and likely encapsulated in carbon (as circled yellow in Fig. S8a). This indicates severer Ni deactivation on $LaNiO_3$ and agrees with its lower DRM performance compared to $La_{0.9}Ce_{0.1}NiO_3$. Liu et al. also observed that light irradiation can tune the carbon deposition behavior of the Ni-based catalysts during PTC-DRM process [25].

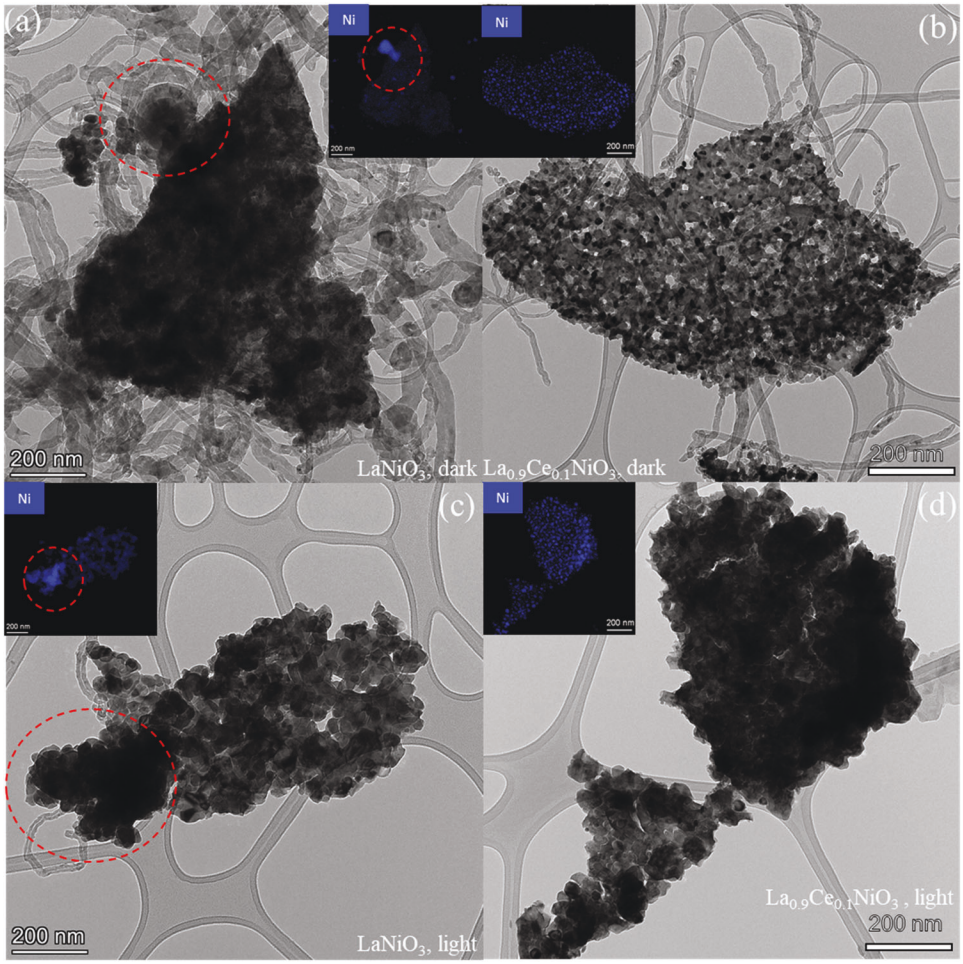


**Fig. 8.** TEM images and Ni element mapping images of spent $LaNiO_3$ and $La_{0.9}Ce_{0.1}NiO_3$ after DRM reaction at 700 °C under the dark and light conditions.

Thermogravimetric mass spectrometric (TGA) analysis and Raman spectroscopy was then performed to determine the deposited coke amount on spent catalysts after DRM reactions under the light and dark conditions (Fig. S9, S10). Specifically, a weight loss of 47.0% and 51.6% was observed on $LaNiO_3$ under light and in the dark condition, respectively. While on $La_{0.9}Ce_{0.1}NiO_3$, the values reduced to 20.2% and 27.6%. The difference in coke formation amounts on the two catalysts agrees with the visual observations on TEM images. With regard to Raman analysis, two peaks, with D band at ~1330 $cm^{-1}$ and G band at ~1580 $cm^{-1}$ were observed on all catalysts, which are assigned to amorphous carbon and graphitic carbon, respectively, where carbon filaments are usually composed of graphitic carbon [25,87]. We calculated the intensity ratios of D- and G-band ($I_D/I_G$) on spent catalysts after DRM reaction at 700 °C under dark and light conditions (Table S3). Clearly, the $I_D/I_G$ ratio is larger under light than that in the dark, and the $I_D/I_G$ ratio of spent $La_{0.9}Ce_{0.1}NiO_3$ is larger than that of spent $LaNiO_3$. The ratio of $I_D/I_G$ is highest on spent $La_{0.9}Ce_{0.1}NiO_3$ under light, while it has the highest DRM performance. The positive correlation of the fraction of amorphous carbon with DRM performance agrees with the literature that amorphous carbon is more reactive and easier to be gasified so that Ni can continuously serve as the active sites for DRM reaction [88,89].

The effect of Ni NPs size on the nucleation and growth of coke in DRM is well reported in the literature [60,90,91]. In our case, the average Ni NP size on fresh $La_{0.9}Ce_{0.1}NiO_3$ and $LaNiO_3$ (16.5 ± 7.3 nm and 12.3 ± 5.7 nm, respectively) are similar, but TEM images indicated the severe agglomeration of Ni NPs on spent $LaNiO_3$. Thus, the partial substitution of Ce can prevent the Ni from aggregation, reducing the coke formation, and thus improving the PTC-DRM activities and stability.

Then, XRD analysis was performed on the spent $La_{0.9}Ce_{0.1}NiO_3$ and $LaNO_3$ and compared with the reduced samples to observe the structure change (Fig. S11). It is clearly observed that on $La_{0.9}Ce_{0.1}NiO_3$, the perovskite $LaNiO_3$ structure was still present after the DRM reactions, while on $LaNiO_3$, the structure was destroyed and became Ni and $La_2O_3$. Similarly, Das et al. reported that the perovskite structure was maintained in the DRM atmosphere by partially substituting Ni with Fe on $La_{0.9}Sr_{0.1}NiO_3$ [60]. Wang et al. also reported that the stability of perovskite $(LaCe)(NiFe)O_3$ structure are credited to the preserved perovskite structure during the DRM reaction environment [36].

Furthermore, we conducted XPS analysis on spent $La_{0.9}Ce_{0.1}NiO_3$ after DRM reaction at 700 °C under the dark and light conditions and presented the deconvolution of O 1 S XPS spectra in Fig. S12. Similar to that observed in Fig. 4, two types of oxygen species, lattice oxygen ($O_L$) at ~530 eV, and chemisorbed oxygen ($O_A$) related to the presence of oxygen vacancies ($V_O$) at ~532 eV, were identified. By calculating the peak area ratio, the $O_A$ concentration value was determined to be 58.6% and 73.3% under the dark and light conditions, respectively, both are lower than the value of fresh $La_{0.9}Ce_{0.1}NiO_3$ (82.0%), indicating the consumption of $V_O$ during reaction process. More importantly, the higher $V_O$ concentration under light can possibly enhance $CO_2$ adsorption and the adsorbed O on $V_O$ can oxidize deposited coke, thus improved PTC-DRM activity and stability were achieved under light condition. Several other publications also reported that light illumination can induce the generation of $V_O$ on $CeO_2$ [12,49,92], $SrTiO_3$ [93], or $TiO_2$ [94], because photogenerated electrons may weaken and break

metal-O bonds.

### 3.5. Photothermalchemical DRM reaction mechanism

Multiple compositions are responsible for the enhanced PTC-DRM activities on $La_{0.9}Ce_{0.1}NiO_3$. The effects of Ni metallic phase, $CeO_2$, and perovskite structure $LaNiO_3$ are thus discussed.

The Ni metallic phase is undoubtedly the primary catalytic site for PTC-DRM reaction, and previous study also confirmed that performance on Ni-free supports was extremely poor [6,7]. Our TEM analysis indicated that Ni NPs were uniformly distributed on $La_{0.9}Ce_{0.1}NiO_3$, and the aggregation of Ni NPs was mitigated during the reaction. It is likely that the Ce promoter reduced the chemical interaction between Ni and support, leading to increased reducibility, evidenced by $H_2$-TPR results (Fig. 1), thus better dispersion of Ni [95]. The tiny Ni NPs enhanced the $CH_4$ conversion and the interaction of Ni-ceria improved $CH_x$ oxidization, avoiding complete decomposition of $CH_x$ to carbon, thus less carbon was observed on $La_{0.9}Ce_{0.1}NiO_3$ [96,97]. Ye et al. also reported that Ni LSPR property enhances PTC-DRM activities with smaller particle size, while large Ni particles can lead to weak optical property [22]. The light absorption on $La_{0.9}Ce_{0.1}NiO_3$ extended to light of visible and near infra-red region, therefore it can strongly harvest solar energy and the PTC-DRM activities under light irradiation was significantly boosted.

$CeO_2$ was reported to generate electron-hole pairs and oxygen vacancies under light irradiation [7,12]. $CO_2$ adsorption and conversion can happen on oxygen vacancies to produce CO, and $CH_4$ or intermediates ($CH_x$) can be oxidized to produce CO and $H_2$, thus PTC-DRM activities were highly enhanced by $CeO_2$. As indicated from the O 1 s XPS spectra (Fig. 4), oxygen vacancies concentrations are much higher on $La_{0.9}Ce_{0.1}NiO_3$ than $LaNiO_3$, and the light absorption ability is also stronger on $La_{0.9}Ce_{0.1}NiO_3$ (Fig. 5). Therefore, it is likely that the Ce partial substitution retains the perovskite structure in the DRM environment, and the generated oxygen vacancies and electrons can boost $CO_2$ adsorption and activation, thus promoting the generation of active intermediate $La_2O_2CO_3$ to mitigate carbon formation and boost the DRM activities. However, for Ce-rich catalysts (x = 0.5, 1), although higher values of oxygen storage capacity were obtained, they showed declined activities. Therefore, $CeO_2$ functions as an optimal promoter at a lower concentration (x = 0.1).

The perovskite structure can also be the active sites, in which the dominant defects during DRM process are oxygen vacancies, which can act as the active sites for adsorption and activation of the reactants and intermediates [36]. In our study, the observed preservation of perovskite structure on $La_{0.9}Ce_{0.1}NiO_3$ is likely benefited by two factors: (1) replenishment of oxygen vacancies from Ce substitution; (2) uniform distribution of Ni to boost the oxidation process [60,98].

For comparison purpose, the $La_{0.9}Ce_{0.1}$ oxides supports were first synthesized, and same amount of Ni was wet impregnated on the supports to yield $Ni/La_{0.9}Ce_{0.1}O_x$. By conducting PTC-DRM on $La_{0.9}Ce_{0.1}NiO_3$ and $Ni/La_{0.9}Ce_{0.1}NiO_x$ at the same DRM reaction conditions (Fig. S12), it was found that $Ni/La_{0.9}Ce_{0.1}NiO_x$ received inefficient and unstable PTC-DRM performance, proving the catalytic properties of perovskite structure. The perovskite catalyst was also widely used in photocatalytic $CO_2$ reduction since it has strong light absorption and can generate electron-hole pairs for $CO_2$ reduction at surface sites [99].

Additionally, to verify the potential photocatalysis on $La_{0.9}Ce_{0.1}NiO_3$ in the solar-driven DRM process, a control experiment was conducted at 700 °C with a 495 nm long-pass filter applied. The comparison of 10 h average DRM performance of $La_{0.9}Ce_{0.1}NiO_3$ under full spectrum, 495 nm long-pass filter, and dark conditions was presented in the Table 2. The DRM performance is almost the same under the 495 nm long-pass filter and dark conditions, indicating the existence of photocatalysis that boosted the DRM reaction on $La_{0.9}Ce_{0.1}NiO_3$ under full spectrum irradiation.

Based on the above experimental results and discussion, the possible PTC-DRM reaction pathways on $La_{1-x}Ce_xNiO_3$ catalyst are proposed as follows: $CH_4$ dissociation takes place on Ni reaction sites to form C* and H* intermediates (Steps 1–2) [60]. Two H* can couple and form $H_2$ (Step 3), and C* can be oxidized by lattice oxygen ($O_L$) to generate CO (Step 4). On the other hand, $CO_2$ can directly dissociate over oxygen vacancies ($V_O$) or hydrogenate yielding CO, O, carbonate, or formate as intermediates (Steps 5–7), which can further react to form CO (Steps 8–9) [100–102]. $CO_2$ can also be adsorbed on the $La_2O_3$ surface and subsequently convert $La_2O_3$ into $La_2O_2CO_3$ intermediate, which can actively react with deposited coke (Steps 10–11) [100,103]. Additionally, under light illumination, high-energy electron ($e^-$) and holes ($h^+$) will be generated on the perovskite catalysts [11,31,69]. The $e^-$ can generate $V_O$ on the catalyst surface and enhance the CO production, while $h^+$ can boost $CH_4$ dissociation towards higher $H_2$ production (Steps 12–14).

**Table 2**
DRM performance of $La_{0.9}Ce_{0.1}NiO_3$ under different light irradiation conditions at 700 °C.

| Reaction conditions | $H_2$ production rate (mmol $g^{-1}$ $h^{-1}$) | CO production rate (mmol $g^{-1}$ $h^{-1}$) |
|---|---|---|
| Full Spectrum | 620 | 616 |
| > 495 nm pass filter | 554 | 548 |
| Dark | 545 | 550 |

$$CH_4 \rightarrow CH_x^* + (4-x)H^* \quad (1)$$

$$CH \rightarrow C^* + H^* \quad (2)$$

$$2\,H^* \rightarrow H_2 \quad (3)$$

$$C^* + O_L \rightarrow CO + V_O \quad (4)$$

$$CO_2 + V_O \rightarrow CO + O_L \quad (5)$$

$$CO_2 + H^* \rightarrow HCOO^* \quad (6)$$

$$CO_2 + O_L \rightarrow CO_3^{2-} \quad (7)$$

$$HCOO^* \rightarrow CO + OH^* \quad (8)$$

$$CO_3^{2-} + C^* \rightarrow 2CO + O_L \quad (9)$$

$$La_2O_3 + CO_2 \rightarrow La_2O_2CO_3 \quad (10)$$

$$C^* + La_2O_2CO_3 \rightarrow 2CO + La_2O_3 \quad (11)$$

$$La_xCe_{1-x}NiO_3 + hv \rightarrow e^- + h^+ \quad (12)$$

$$Ce^{4+} + e^- \rightarrow Ce^{3+} + V_O + O \quad (13)$$

$$CH_4 + xh^+ \rightarrow CH_{(4-x)} + xH^+ \quad (14)$$

## 4. Conclusion

In summary, promoting effects of partial substitution of Ce into $LaNiO_3$ perovskite catalysts on the PTC-DRM activities were presented. Ce, as a promoter, was found to benefit Ni NPs active sites distribution and perovskite structure retention on $La_{0.9}Ce_{0.1}NiO_3$. Therefore, Ni aggregation can be mitigated during PTC-DRM process due to stronger metal-support interaction. In addition, by conducting in situ DRIFTS analysis and control experiment with 495 nm long-pass filter, the light irradiation was found to enhance $CO_2$ adsorption and formation of active intermediate $La_2O_2CO_3$, induce photocatalytic activities on $La_{0.9}Ce_{0.1}NiO_3$, assisted by generated oxygen vacancies and electron-hole pairs. These advantages led to carbon mitigation and promoted PTC-DRM activities. As a result, at 700 °C under 30 suns light irradiation, the $La_{0.9}Ce_{0.1}NiO_3$ showed highest PTC-DRM activities with CO

and $H_2$ production rates of 616 and 620 mmol $g^{-1}$ $h^{-1}$, respectively. This work systematically advances the design of cost-effective catalysts and the study of the light contribution mechanism thus promoting efficient solar-powered conversion of greenhouse gases.

## CRediT authorship contribution statement

**Zichen Du:** Conceptualization, Methodology, Software, Validation, Formal analysis, Investigation, Data curation, Writing – original draft, Visualization, Writing – review & editing. **Cullen Petru:** Investigation, Methodology, Writing – review & editing. **Xiaokun Yang:** Validation, Resources, Writing – review & editing. **Fan Chen***:* Validation, Resources. **Siyuan Fang:** Validation, Resources. **Fuping Pan:** Validation, Writing – review & editing. **Yang Gang:** Validation, Writing – review & editing. **Hong-Cai Zhou:** Resources, Writing – review & editing. **Yun Hang Hu:** Resources, Writing – review & editing. **Ying Li:** Conceptualization, Writing – review & editing, Supervision, Project administration, Funding acquisition.

## Declaration of Competing Interest

The authors declare that they have no known competing financial interests or personal relationships that could have appeared to influence the work reported in this paper.

## Data Availability

Data will be made available on request.

## Acknowledgements

This work was supported by U.S. National Science Foundation (Grant No. 1924466). The use of Materials Characterization Facility (MCF) at Texas A&M University is acknowledged.

*Supporting Information*

Reactor configuration, irradiation spectrum of concentrated solar, additional PTC-DRM activities comparison, in situ DRIFTS spectra, TGA, XRD, Raman characterization.

## Appendix A. Supporting information

Supplementary data associated with this article can be found in the online version at doi:10.1016/j.jcou.2022.102317.

## References

[1] Z.J. Wang, H. Song, H.M. Liu, J.H. Ye, Coupling of solar energy and thermal energy for carbon dioxide reduction: status and prospects, Angew. Chem. Int Ed. 59 (2020) 8016–8035.
[2] N.A.K. Aramouni, J.G. Touma, B. Abu Tarboush, J. Zeaiter, M.N. Ahmad, Catalyst design for dry reforming of methane: analysis review, Renew. Sust. Energ. Rev. 82 (2018) 2570–2585.
[3] A.H.B. Mostaghimi, T.A. Al-Attas, M.G. Kibria, S. Siahrostami, A review on electrocatalytic oxidation of methane to oxygenates, J. Mater. Chem. A 8 (2020) 15575–15590.
[4] Q.J. Zhu, S.L. Wegener, C. Xie, O. Uche, M. Neurock, T.J. Marks, Sulfur as a selective 'soft' oxidant for catalytic methane conversion probed by experiment and theory, Nat. Chem. 5 (2013) 104–109.
[5] C. Agrafiotis, H. von Storch, M. Roeb, C. Sattler, Solar thermal reforming of methane feedstocks for hydrogen and syngas production-a review, Renew. Sust. Energ. Rev. 29 (2014) 656–682.
[6] M.J. Li, Z.X. Sun, Y.H. Hu, Thermo-photo coupled catalytic $CO_2$ reforming of methane: a review, Chem. Eng. J. 428 (2022), 131222.
[7] Z. Du, F. Pan, X. Yang, L. Fang, Y. Gang, S. Fang, T. Li, Y.H. Hu, Y.J.C.T. Li, Efficient photothermochemical dry reforming of methane over Ni supported on ZrO2 with CeO2 incorporation, Catal. Today (2022), https://doi.org/10.1016/j.cattod.2022.05.014.
[8] X.H. Feng, Z.C. Du, E. Sarnello, W. Deng, C.R. Petru, L.Z. Fang, T. Li, Y. Li, Syngas production at a near-unity H-2/CO ratio from photo-thermo-chemical dry reforming of methane on a Pt decorated Al2O3-CeO2 catalyst, J. Mater. Chem. A 10 (2022) 7896–7910.
[9] K.H. Han, Y. Wang, S. Wang, Q.Y. Liu, Z.Y. Deng, F.G. Wang, Narrowing band gap energy of CeO2 in (Ni/CeO2)@SiO2 catalyst for photothermal methane dry reforming, Chem. Eng. J. 421 (2021), 129989.
[10] Z.Q. Rao, Y.H. Cao, Z.A. Huang, Z.H. Yin, W.C. Wan, M.Z. Ma, Y.X. Wu, J. B. Wang, G.D. Yang, Y. Cui, Z.M. Gong, Y. Zhou, Insights into the nonthermal effects of light in dry reforming of methane to enhance the H-2/CO ratio near unity over Ni/Ga2O3, Acs Catal. 11 (2021) 4730–4738.
[11] T. Xie, Z.Y. Zhang, H.Y. Zheng, K.D. Xu, Z. Hu, Y. Lei, Enhanced photothermal catalytic performance of dry reforming of methane over Ni/mesoporous TiO2 composite catalyst, Chem. Eng. J. 429 (2022), 132507.
[12] F.P. Pan, X.M. Xiang, Z.C. Du, E. Sarnello, T. Li, Y. Li, Integrating photocatalysis and thermocatalysis to enable efficient $CO_2$ reforming of methane on Pt supported CeO2 with Zn doping and atomic layer deposited MgO overcoating, Appl. Catal. B-Environ. 260 (2020), 118189.
[13] Z.Z. Zhu, W.Y. Guo, Y. Zhang, C.S. Pan, J. Xu, Y.F. Zhu, Y. Lou, Research progress on methane conversion coupling photocatalysis and thermocatalysis, Carbon Energy 3 (2021) 519–540.
[14] F.P. Pan, X.M. Xiang, Z.C. Du, E. Sarnello, T. Li, Y. Li, Integrating photocatalysis and thermocatalysis to enable efficient $CO_2$ reforming of methane on Pt supported CeO2 with Zn doping and atomic layer deposited MgO overcoating, Appl. Catal. B-Environ. 260 (2020) 118–189.
[15] B. Han, W. Wei, L. Chang, P.F. Cheng, Y.H. Hu, Efficient visible light photocatalytic $CO_2$ reforming of CH4, ACS Catal. 6 (2016) 494–497.
[16] F.P. Pan, X.M. Xiang, W. Deng, H.L. Zhao, X.H. Feng, Y. Li, A novel photo-thermochemical approach for enhanced carbon dioxide reforming of methane, Chemcatchem 10 (2018) 940–945.
[17] H. Song, X. Meng, T.D. Dao, W. Zhou, H. Liu, L. Shi, H. Zhang, T. Nagao, T. Kako, J. Ye, Light-enhanced carbon dioxide activation and conversion by effective plasmonic coupling effect of Pt and Au nanoparticles, ACS Appl. Mater. Inter 10 (2018) 408–416.
[18] L.A. Zhou, J.M.P. Martirez, J. Finzel, C. Zhang, D.F. Swearer, S. Tian, H. Robatjazi, M.H. Lou, L.L. Dong, L. Henderson, P. Christopher, E.A. Carter, P. Nordlander, N.J. Halas, Light-driven methane dry reforming with single atomic site antenna-reactor plasmonic photocatalysts, Nat. Energy 5 (2020) 61–70.
[19] S. Shoji, X.B. Peng, A. Yamaguchi, R. Watanabe, C. Fukuhara, Y. Cho, T. Yamamoto, S. Matsumura, M.W. Yu, S. Ishii, T. Fujita, H. Abe, M. Miyauchi, Photocatalytic uphill conversion of natural gas beyond the limitation of thermal reaction systems, Nat. Catal. 3 (2020) 148–153.
[20] H.M. Liu, M. Li, T.D. Dao, Y.Y. Liu, W. Zhou, L.Q. Liu, X.G. Meng, T. Nagao, J. H. Ye, Design of PdAu alloy plasmonic nanoparticles for improved catalytic performance in $CO_2$ reduction with visible light irradiation, Nano Energy 26 (2016) 398–404.
[21] G.Q. Zhang, S.W. Wu, Y.Z. Li, Q. Zhang, Significant improvement in activity, durability, and light-to-fuel efficiency of Ni nanoparticles by La2O3 cluster modification for photothermocatalytic $CO_2$ reduction, Appl. Catal. B-Environ. 264 (2020), 118544.
[22] H.M. Liu, H. Song, X.G. Meng, L.Q. Yang, J.H. Ye, Light irradiation enhanced $CO_2$ reduction with methane: A case study in size-dependent optical property of Ni nanoparticles, Catal. Today 335 (2019) 187–192.
[23] H. Huang, M. Mao, Q. Zhang, Y. Li, J. Bai, Y. Yang, M. Zeng, X. Zhao, Solar-light-driven $CO_2$ reduction by CH4 on silica-cluster-modified Ni nanocrystals with a high solar-to-fuel efficiency and excellent durability, Adv. Energy Mater. 8 (2018) 1702472.
[24] Q. Zhang, M.Y. Mao, Y.Z. Li, Y. Yang, H. Huang, Z.K. Jiang, Q.Q. Hu, S.W. Wu, X. J. Zhao, Novel photoactivation promoted light-driven $CO_2$ reduction by CH4 on Ni/CeO2 nanocomposite with high light-to-fuel efficiency and enhanced stability, Appl. Catal. B-Environ. 239 (2018) 555–564.
[25] H.M. Liu, X.G. Meng, T.D. Dao, L.Q. Liu, P. Li, G.X. Zhao, T. Nagao, L.Q. Yang, J. H. Ye, Light assisted $CO_2$ reduction with methane over SiO2 encapsulated Ni nanocatalysts for boosted activity and stability, J. Mater. Chem. A 5 (2017) 10567–10573.
[26] H.M. Liu, T.D. Dao, L.Q. Liu, X.G. Meng, T. Nagaoa, J.H. Ye, Light assisted $CO_2$ reduction with methane over group VIII metals: universality of metal localized surface plasmon resonance in reactant activation, Appl. Catal. B-Environ. 209 (2017) 183–189.
[27] S.W. Wu, Y.Z. Li, Q. Zhang, Q.Q. Hu, J.C. Wu, C.Y. Zhou, X.J. Zhao, Formation of NiCo alloy nanoparticles on Co doped Al(2)O(3)leads to high fuel production rate, large light-to-fuel efficiency, and excellent durability for photothermocatalytic CO(2)reduction, Adv. Energy Mater. 10 (2020) 2002602.
[28] G.Q. Zhang, S.W. Wu, Y.Z. Li, Q. Zhang, Significant improvement in activity, durability, and light-to-fuel efficiency of Ni nanoparticles by La2O3 cluster modification for photothermocatalytic $CO_2$ reduction, Appl. Catal. B-Environ. 264 (2020) 118–544.
[29] H. Huang, M. Mao, Q. Zhang, Y. Li, J. Bai, Y. Yang, M. Zeng, X. Zhao, Solar-Light-Driven CO2 Reduction by CH4 on Silica-Cluster-Modified Ni Nanocrystals with a High Solar-to-Fuel Efficiency and Excellent Durability, 8 (2018) 1702472.
[30] B. Abdullah, N.A.A. Ghani, D.V.N. Vo, Recent advances in dry reforming of methane over Ni-based catalysts, J. Clean. Prod. 162 (2017) 170–185.
[31] M. Tahir, B. Tahir, Z.Y. Zakaria, A. Muhammad, Enhanced photocatalytic carbon dioxide reforming of methane to fuels over nickel and montmorillonite supported TiO2 nanocomposite under UV-light using monolith photoreactor, J. Clean. Prod. 213 (2019) 451–461.

[32] K. Lorber, J. Zavasnik, J. Sancho-Parramon, M. Bubas, M. Mazaj, P. Djinovic, On the mechanism of visible-light accelerated methane dry reforming reaction over Ni/CeO2-x catalysts, Appl. Catal. B-Environ. 301 (2022), 120745.
[33] L.G. Tejuca, J.L. Fierro, Properties and Applications of Perovskite-type Oxides, CRC Press, 1992.
[34] G. Valderrama, M.R. Goldwasser, C.U. de Navarro, J.M. Tatibouet, J. Barrault, C. Batiot-Dupeyrat, F. Martinez, Dry reforming of methane over Ni perovskite type oxides, Catal. Today, 107- 08 (2005) 785–791.
[35] E. le Sache, L. Pastor-Perez, D. Watson, A. Sepulveda-Escribano, T.R. Reina, Ni stabilised on inorganic complex structures: superior catalysts for chemical $CO_2$ recycling via dry reforming of methane, Appl. Catal. B-Environ. 236 (2018) 458–465.
[36] M. Wang, T.T. Zhao, X.L. Dong, M. Li, H.Q. Wang, Effects of Ce substitution at the A-site of LaNi0.5Fe0.5O3 perovskite on the enhanced catalytic activity for dry reforming of methane, Appl. Catal. B-Environ. 224 (2018) 214–221.
[37] S. Joo, A. Seong, O. Kwon, K. Kim, J.H. Lee, R.J. Gorte, J.M. Vohs, J.W. Han, G. Kim, Highly active dry methane reforming catalysts with boosted in situ grown Ni-Fe nanoparticles on perovskite via atomic layer deposition, Sci. Adv. 6 (2020) eabb1573.
[38] L.S. Gangurde, G.S.J. Sturm, M.J. Valero-Romero, R. Mallada, J. Santamaria, A. I. Stankiewicz, G.D. Stefanidis, Synthesis, characterization, and application of ruthenium-doped SrTiO3 perovskite catalysts for microwave-assisted methane dry reforming, Chem. Eng. Process 127 (2018) 178–190.
[39] F. Touahra, R. Chebout, D. Lerari, D. Halliche, K. Bachari, Role of the nanoparticles of Cu-Co alloy derived from perovskite in dry reforming of methane, Energy 171 (2019) 465–474.
[40] X.Z. Li, H.Y. Shi, W. Zhu, S.X. Zuo, X.W. Lu, S.P. Luo, Z.Y. Li, C. Yao, Y.S. Chen, Nanocomposite LaFe1-xNixO3/Palygorskite catalyst for photo-assisted reduction of NOx: Effect of Ni doping, Appl. Catal. B-Environ. 231 (2018) 92–100.
[41] A. Kumar, A. Kumar, V. Krishnan, Perovskite oxide based materials for energy and environment-oriented photocatalysis, ACS Catal. 10 (2020) 10253–10315.
[42] E.M. Akinoglu, D.A. Hoogeveen, C. Cao, A.N. Simonov, J.J. Jasieniak, Prospects of Z-scheme photocatalytic systems based on metal halide perovskites, ACS Nano 15 (2021) 7860–7878.
[43] S. Purohit, K.L. Yadav, S. Satapathi, Bandgap engineering in a staggered-type oxide perovskite heterojunction for efficient visible light-driven photocatalytic dye degradation, Langmuir 37 (2021) 3467–3476.
[44] A. Kumar, V.N. Rao, A. Kumar, A. Mushtaq, L. Sharma, A. Halder, S.K. Pal, M. V. Shankar, V. Krishnan, Three-dimensional carbonaceous aerogels embedded with Rh-SrTiO3 for enhanced hydrogen evolution triggered by efficient charge transfer and light absorption, ACS Appl. Energ. Mater. 3 (2020) 12134–12147.
[45] H. Provendier, C. Petit, C. Estournes, A. Kiennemann, Dry reforming of methane. Interest of La-Ni-Fe solid solutions compared to LaNiO3 and LaFeO3, Stud. Surf. Sci. Catal. 119 (1998) 741–746.
[46] S. Bhattar, M.A. Abedin, S. Kanitkar, J.J. Spivey, A review on dry reforming of methane over perovskite derived catalysts, Catal. Today 365 (2021) 2–23.
[47] G. Valderrama, C.U. de Navarro, M.R. Goldwasser, $CO_2$ reforming of CH4 over Co-La-based perovskite-type catalyst precursors, J. Power Sources 234 (2013) 31–37.
[48] J.D.G. Fernandes, D.M.A. Melo, L.B. Zinner, C.M. Salustiano, Z.R. Silva, A. E. Martinelli, M. Cerqueira, C.A. Junior, E. Longo, M.I.B. Bernardi, Low-temperature synthesis of single-phase crystalline LaNiO3 perovskite via Pechini method, Mater. Lett. 53 (2002) 122–125.
[49] Z.C. Du, F.P. Pan, E. Sarnello, X.H. Feng, Y. Gang, T. Li, Y. Li, Probing the origin of photocatalytic effects in photothermochemical dry reforming of methane on a Pt/CeO2 catalyst, J. Phys. Chem. C. 125 (2021) 18684–18692.
[50] E.H. Yang, N.Y. Kim, Y.S. Noh, S.S. Lim, J.S. Jung, J.S. Lee, G.H. Hong, D.J. Moon, Steam $CO_2$ reforming of methane over La1-xCexNiO3 perovskite catalysts, Int J. Hydrog. Energ. 40 (2015) 11831–11839.
[51] M. Surendar, T.V. Sagar, G. Raveendra, M.A. Kumar, N. Lingaiah, K.S.R. Rao, P.S. S. Prasad, Pt doped LaCoO3 perovskite: a precursor for a highly efficient catalyst for hydrogen production from glycerol, Int. J. Hydrog. Energ. 41 (2016) 2285–2297.
[52] G. Valderrama, A. Kiennemann, M.R. Goldwasser, Dry reforming of CH4 over solid solutions of LaN1-xCoxO3, Catal. Today 133 (2008) 142–148.
[53] Y. Cui, V. Galvita, L. Rihko-Struckmann, H. Lorenz, K. Sundmacher, Steam reforming of glycerol: The experimental activity of La1-xCexNiO3 catalyst in comparison to the thermodynamic reaction equilibrium, Appl. Catal. B-Environ. 90 (2009) 29–37.
[54] J.M. Naik, C. Ritter, B. Bulfin, A. Steinfeld, R. Erni, G.R. Patzke, Reversible phase transformations in novel ce-substituted perovskite oxide composites for solar thermochemical redox splitting of $CO_2$, Adv. Energy Mater. 11 (2021) 2003532.
[55] A. Kambolis, H. Matralis, A. Trovarelli, C. Papadopoulou, Ni/CeO2-ZrO2 catalysts for the dry reforming of methane, Appl. Catal. a-Gen. 377 (2010) 16–26.
[56] C.A. Franchini, W. Aranzaez, A.M.D. de Farias, G. Pecchi, M.A. Fraga, Ce-substituted LaNiO3 mixed oxides as catalyst precursors for glycerol steam reforming, Appl. Catal. B-Environ. 147 (2014) 193–202.
[57] K. Soongprasit, D. Aht-Ong, V. Sricharoenchaikul, D. Atong, Synthesis and catalytic activity of sol-gel derived La-Ce-Ni perovskite mixed oxide on steam reforming of toluene, Curr. Appl. Phys. 12 (2012) S80–S88.
[58] Y. Wang, G.F. Zhang, C.S. Li, G. Yan, Y.F. Lu, Preparation and characterization of LaNiO3 films grown by metal-organic deposition, B Mater. Sci. 34 (2011) 1379–1383.
[59] A. Abdulrasheed, A.A. Jalil, Y. Gambo, M. Ibrahim, H.U. Hambali, M.Y.S. Hamill, A review on catalyst development for dry reforming of methane to syngas: recent advances, Renew. Sust. Energ. Rev. 108 (2019) 175–193.
[60] S. Das, S. Bhattar, L.N. Liu, Z.G. Wang, S.B. Xi, J.J. Spivey, S. Kawi, Effect of partial Fe substitution in La0.9Sr0.1NiO3 perovskite-derived catalysts on the reaction mechanism of methane dry reforming, ACS Catal. 10 (2020) 12466–12486.
[61] G.P. Figueredo, R.L.B.A. Medeiros, H.P. Macedo, A.A.S. de Oliveira, R.M. Braga, J.M.R. Mercury, M.A.F. Melo, D.M.A. Melo, A comparative study of dry reforming of methane over nickel catalysts supported on perovskite-type LaAlO3 and commercial alpha-Al2O3, Int J. Hydrog. Energ. 43 (2018) 11022–11037.
[62] X.M. Xiang, H.H. Zhao, J. Yang, J. Zhao, L. Yan, H.L. Song, L.J. Chou, Nickel based mesoporous silica-ceria-zirconia composite for carbon dioxide reforming of methane, Appl. Catal. a-Gen. 520 (2016) 140–150.
[63] B. Safavinia, Y.M. Wang, C.Y. Jiang, C. Roman, P. Darapaneni, J. Larriviere, D. A. Cullen, K.M. Dooley, J.A. Dorman, Enhancing CexZr1-xO2 activity for methane dry reforming using subsurface Ni dopants, ACS Catal. 10 (2020) 4070–4079.
[64] J.Y. Chen, Z.G. He, G.Y. Li, T.C. An, H.X. Shi, Y.Z. Li, Visible-light-enhanced photothermocatalytic activity of ABO(3)-type perovskites for the decontamination of gaseous styrene, Appl. Catal. B-Environ. 209 (2017) 146–154.
[65] A. Ghafoor, I. Bibi, F. Majid, S. Kamal, S. Ata, N. Nazar, M. Iqbal, M.A.S. Raza, M. M. Almoneef, Ce and Fe doped LaNiO3 synthesized by micro-emulsion route: Effect of doping on visible light absorption for photocatalytic application, Mater. Res. Express 8 (2021), 085009.
[66] L.J. An, H. Onishi, Electron-hole recombination controlled by metal doping sites in NaTaO3 photocatalysts, Acs Catal. 5 (2015) 3196–3206.
[67] M. Anas, D.S. Han, K. Mahmoud, H. Park, A. Abdel-Wahab, Photocatalytic degradation of organic dye using titanium dioxide modified with metal and non-metal deposition, Mat. Sci. Semicon Proc. 41 (2016) 209–218.
[68] J.Q. Zhang, Y.G. Li, J.M. Sun, H.J. Chen, Y.Z. Zhu, X.L. Zhao, L.C. Zhang, S. J. Wang, H.Y. Zhang, X.G. Duan, L. Shi, S. Zhang, P. Zhang, G.S. Shao, M.B. Wu, S. B. Wang, H.Q. Sun, Regulation of energetic hot carriers on Pt/TiO2 with thermal energy for photothermal catalysis, Appl. Catal. B-Environ. 309 (2022), 121263.
[69] Z.Y. Zhang, T. Zhang, W.P. Liang, P.W. Bai, H.Y. Zheng, Y. Lei, Z. Hu, T. Xie, Promoted solar-driven dry reforming of methane with Pt/mesoporous-TiO2 photo-thermal synergistic catalyst: performance and mechanism study, Energ. Convers. Manag. 258 (2022), 115496.
[70] T.T. Zhang, Z.X. Liu, Y.A. Zhu, Z.C. Liu, Z.J. Sui, K.K. Zhu, X.G. Zhou, Dry reforming of methane on Ni-Fe-MgO catalysts: influence of Fe on carbon-resistant property and kinetics, Appl. Catal. B-Environ. 264 (2020), 118497.
[71] K. Song, M.M. Lu, S.P. Xu, C.Q. Chen, Y.Y. Zhan, D.L. Li, C. Au, L.L. Jiang, K. Tomishige, Effect of alloy composition on catalytic performance and coke-resistance property of Ni-Cu/Mg(Al)O catalysts for dry reforming of methane, Appl. Catal. B-Environ. 239 (2018) 324–333.
[72] J. Dou, R.G. Zhang, X.B. Hao, Z.H. Bao, T.P. Wu, B.J. Wang, F. Yu, Sandwiched SiO2@Ni@ZrO2 as a coke resistant nanocatalyst for dry reforming of methane, Appl. Catal. B-Environ. 254 (2019) 612–623.
[73] K.H. Han, S. Wang, Q.Y. Liu, F.G. Wang, Optimizing the Ni/Cu ratio in Ni-Cu nanoparticle catalysts for methane dry reforming, Acs Appl. Nano Mater. 4 (2021) 5340–5348.
[74] P.J. Linstrom, W.G. Mallard (Eds.), NIST Chemistry WebBook, NIST Standard Reference Database Number 69, 20899, National Institute of Standards and Technology, Gaithersburg MD, 2020.
[75] L.F. Bobadilla, V. Garcilaso, M.A. Centeno, J.A. Odriozola, Monitoring the reaction mechanism in model biogas reforming by insitu transient and steady-state DRIFTS measurements, Chemsuschem 10 (2017) 1193–1201.
[76] C.M. Kalamaras, D.D. Dionysiou, A.M. Efstathiou, Mechanistic studies of the water-gas shift reaction over Pt/CexZr1-xO2 catalysts: the effect of Pt particle size and Zr dopant, ACS Catal. 2 (2012) 2729–2742.
[77] T. Takeguchi, S. Manabe, R. Kikuchi, K. Eguchi, T. Kanazawa, S. Matsumoto, W. Ueda, Determination of dispersion of precious metals on CeO2-containing supports, Appl. Catal. a-Gen. 293 (2005) 91–96.
[78] W. Bi, Y.J. Hu, N. Jiang, L. Zhang, H. Jiang, X. Zhao, C.Y. Wang, C.Z. Li, Ultra-fast construction of plaque-like Li2TiO3/TiO2 heterostructure for efficient gas-solid phase $CO_2$ photoreduction, Appl. Catal. B-Environ. 269 (2020), 118810.
[79] L.J. Liu, Y.Q. Jiang, H.L. Zhao, J.T. Chen, J.L. Cheng, K.S. Yang, Y. Li, Engineering coexposed {001} and {101} facets in oxygen-deficient TiO2 nanocrystals for enhanced $CO_2$ photoreduction under visible light, ACS Catal. 6 (2016) 1097–1108.
[80] K. Sutthiumporn, S. Kawi, Promotional effect of alkaline earth over Ni-La2O3 catalyst for $CO_2$ reforming of CH4: Role of surface oxygen species on H-2 production and carbon suppression, Int. J. Hydrog. Energ. 36 (2011) 14435–14446.
[81] V.A. Tsipouriari, X.E. Verykios, Kinetic study of the catalytic reforming of methane with carbon dioxide to synthesis gas over Ni/La2O3 catalyst, Catal. Today 64 (2001) 83–90.
[82] K.K. Mandari, H.P. Aytam, S. Varimalla, V.K. Velisoju, V. Akula, Evaluation of in-situ formed La2O3–TiO2–La2O2CO3 nanocomposite photocatalyst for H2 production, Int J. Hydrog. Energ. (2022) 17214–17223.
[83] Y. Gao, Q. Li, C. Wang, D.-X. Yan, J. Chen, H. Jia, Light-driven efficient dry reforming of methane over Pt/La2O3 with long-time durability, J. Mater. Chem. A (2022) 16016–16028.
[84] M.S. Li, A.C. van Veen, Tuning the catalytic performance of Ni-catalysed dry reforming of methane and carbon deposition via Ni-CeO2-x interaction, Appl. Catal. B-Environ. 237 (2018) 641–648.
[85] X.L. Yan, T. Hu, P. Liu, S. Li, B.R. Zhao, Q. Zhang, W.Y. Jiao, S. Chen, P.F. Wang, J.J. Lu, L.M. Fan, X.N. Deng, Y.X. Pan, Highly efficient and stable Ni/CeO2-SiO2 catalyst for dry reforming of methane: effect of interfacial structure of Ni/CeO2 on SiO2, Appl. Catal. B-Environ. 246 (2019) 221–231.

[86] M. Kosari, S. Askari, A.M. Seayad, S. Xi, S. Kawi, A. Borgna, H. Zeng, Strong coke-resistance spherical hollow Ni/SiO2 catalysts with shell-confined high-content ni nanoparticles for methane dry reforming with $CO_2$, Appl. Catal. B-Environ. (2022), 121360.
[87] S. Dama, S.R. Ghodke, R. Bobade, H.R. Gurav, S. Chilukuri, Active and durable alkaline earth metal substituted perovskite catalysts for dry reforming of methane, Appl. Catal. B-Environ. 224 (2018) 146–158.
[88] J. Deng, K.K. Bu, Y.J. Shen, X.Y. Zhang, J.P. Zhang, K. Faungnawakij, D.S. Zhang, Cooperatively enhanced coking resistance via boron nitride coating over Ni-based catalysts for dry reforming of methane, Appl. Catal. B-Environ. 302 (2022), 120859.
[89] I.V. Yentekakis, P. Panagiotopoulou, G. Artemakis, A review of recent efforts to promote dry reforming of methane (DRM) to syngas production via bimetallic catalyst formulations, Appl. Catal. B-Environ. 296 (2021), 120210.
[90] S. Das, A. Jangam, S.B. Xi, A. Borgna, K. Hidajat, S. Kawi, Highly dispersed ni/silica by carbonization-calcination of a chelated precursor for coke-free dry reforming of methane, Acs Appl. Energ. Mater. 3 (2020) 7719–7735.
[91] C.M. Damaskinos, J. Zavasnik, P. Djinovic, A.M. Efstathiou, Dry reforming of methane over Ni/Ce0.8Ti0.2O2-delta: the effect of Ni particle size on the carbon pathways studied by transient and isotopic techniques, Appl. Catal. B-Environ. 296 (2021), 120321.
[92] T. Ye, W.M. Huang, L.M. Zeng, M.L. Li, J.L. Shi, CeO2-x platelet from monometallic cerium layered double hydroxides and its photocatalytic reduction of $CO_2$, Appl. Catal. B-Environ. 210 (2017) 141–148.
[93] X.H. Zhang, L. Zhang, B.W. Deng, J.Y. Jin, C.Y. Xu, Y.W. Zhang, Visible light-responding perovskite oxide catalysts for photo-thermochemical $CO_2$ reduction, Catal. Commun. 138 (2020), 105955.
[94] O. Dulub, M. Batzill, S. Solovev, E. Loginova, A. Alchagirov, T.E. Madey, U. Diebold, Electron-induced oxygen desorption from the TiO2(011)-2×1 surface leads to self-organized vacancies, Science 317 (2007) 1052–1056.
[95] S.B. Wang, G.Q. Lu, Role of CeO2 in Ni/CeO2-Al2O3 catalysts for carbon dioxide reforming of methane, Appl. Catal. B-Environ. 19 (1998) 267–277.
[96] F.G. Wang, L.J. Zhang, J.Q. Deng, J.M. Zhang, B.L. Han, Y. Wang, Z.C. Li, H. Yu, W.J. Cai, Z.Y. Deng, Embedded Ni catalysts in Ni-O-Ce solid solution for stable hydrogen production from ethanol steam reforming reaction, Fuel Process Technol. 193 (2019) 94–101.
[97] F.G. Wang, L.L. Xu, W.D. Shi, Syngas production from $CO_2$ reforming with methane over core-shell Ni@SiO2 catalysts, J. Co2 Util. 16 (2016) 318–327.
[98] J.L.G. Fierro, J.M.D. Tascon, L.G. Tejuca, Surface-properties of Lanio3 - kinetic-studies of reduction and of oxygen-adsorption, J. Catal. 93 (1985) 83–91.
[99] R. Shi, G.I.N. Waterhouse, T.R. Zhang, Recent progress in photocatalytic $CO_2$ reduction over perovskite oxides, Sol. RRL 1 (2017) 1700126.
[100] X.Y. Li, Z.J. Zhao, L. Zeng, J.B. Zhao, H. Tian, S. Chen, K. Li, S. Sang, J.L. Gong, On the role of Ce in $CO_2$ adsorption and activation over lanthanum species, Chem. Sci. 9 (2018) 3426–3437.
[101] J.T. Niu, X.S. Du, J.Y. Ran, R.R. Wang, Dry ($CO_2$) reforming of methane over Pt catalysts studied by DFT and kinetic modeling, Appl. Surf. Sci. 376 (2016) 79–90.
[102] X. Su, X.L. Yang, B. Zhao, Y.Q. Huang, Designing of highly selective and high-temperature endurable RWGS heterogeneous catalysts: recent advances and the future directions, J. Energy Chem. 26 (2017) 854–867.
[103] X.E. Verykios, Catalytic dry reforming of natural gas for the production of chemicals and hydrogen, Int J. Hydrog. Energ. 28 (2003) 1045–1063.